Journal of Sound and Vibration (2001) **247**(2), 195–211
doi:10.1006/jsvi.2000.3482, available online at http://www.idealibrary.com on IDEAL®

PREDICTION AND VALIDATION ON THE SONIC BOOM BY A HIGH-SPEED TRAIN ENTERING A TUNNEL

T. S. YOON, S. LEE, J. H. HWANG AND D. H. LEE

IAAT (Institute of Advanced Aerospace Technology), School of Mechanical and Aerospace Engineering, College of Engineering, Seoul National University, San 56-1 Shilim-Dong, Kwanak-Ku, Seoul 151-742, Korea. E-mail: solee@plaza.snu.ac.kr

(*Received* 26 *May* 2000, *and in final form* 4 *October* 2000)

A compression wave generated when a high-speed train emerges from the exit portal of a tunnel, causes an impulsive noise called micro-pressure wave. There are various countermeasures to reduce the micro-pressure wave, the most effective one being the proper design of the nose shape of the train. In the present study, we adopted a new method for the prediction of sonic boom noise, considering the effect of the nose shape on the resultant noise. The Euler equation is first solved, after which the linear Kirchhoff formulation is used for the prediction of farfield acoustics from the flow-field data.

Experimental investigation is also carried out on the pressure fluctuations in the tunnel and the micro-pressure wave with parameters such as train speed, blockage ratio, nose shape of train and air-shafts. The computational prediction and experimentally measured data, compared in this paper, show a good agreement with each other. The results shows that several countermeasures could be used for the efficient reduction of the micro-pressure wave.

© 2001 Academic Press

1. INTRODUCTION

Some examples of aerodynamic noise sources of a high-speed train are a train nose, cover and pantograph (collecting system) and its cover, cavities of windows, gap noise of the vehicle and tunnel, etc. In low-speed operation, the most dominant sources are rolling and rail noise, but in high-speed operation, aerodynamic noise becomes dominant. Social demand and technological progress together have pushed the speed of trains giving rise to a variety of aerodynamic and aeroacoustic problems.

When a train enters a tunnel at high speed, a compression wave is generated and it propagates along the tunnel. At the tunnel exit, the compression wave is reflected back into the tunnel forming an expansion wave. Such waves create unfavourable aural effects, causing discomfort to passengers when passing through the tunnel. Populations near tunnel exit portals, on the other hand, can suffer from the noise and vibrations (phenomena designated as "sonic boom") caused by the transmission of an impulsive pressure wave called a micro-pressure wave.

The ultimate objective of this research is the reduction of the micro-pressure wave. Therefore, understanding the characteristics of the compression wave and investigating the parameters directly related to the micro-pressure wave are very important. Among conventional methods, a proper design of the nose shape of the train is known to be an important countermeasure in reducing the micro-pressure wave.

In the present study, a new method for predicting the pressure fluctuations in the tunnel and the micro-pressure wave are proposed. Computational fluid dynamics (CFD) technique

0022-460X/01/420195 + 17 $35.00/0 © 2001 Academic Press

is combined with a linear Kirchhoff formulation for computational prediction of the phenomena. An Euler finite difference solver is first executed, from which the nearfield flow data are obtained. The data are then transferred to the linear Kirchhoff formulation to predict the farfield acoustics.

In previous studies, the relation between the micro-pressure wave and compression wave has been derived using the acoustic model of a vibrating circular piston on an infinite baffle plate with low frequency approximation. For example, Ozawa predicted the micro-pressure wave, considering only parameters such as blockage ratio, train speed and tunnel length [1–3]. Since the magnitude of the micro-pressure wave is proportional to the highest pressure gradient of the compression wave arriving at the tunnel exit [4], many numerical methods considering the effect of the nose shape were attempted, to analyze the compression wave at the entrance of the tunnel [5–9].

Experimental investigations were also carried out in the Train Tunnel Test Facility (T3F) a the National Aerospace Laboratory (NLR) in Netherlands under a contract with Seoul National University. The influence of train nose shapes and tunnel configurations on the micro-pressure wave and pressure fluctuations in the tunnel were examined by varying the train speed, blockage ratio and air-shafts. The facility can launch a rig-test train model with an interchangeable nose at velocities up to 500 km/h using a pneumatic launch system. The experimental results are compared with the computationally predicted results. These numerical and experimental studies can be very useful in designing the nose shape and tunnel cross-section that minimize the ringing in passengers' ears and the sonic boom. The studies are also important to understand the physical phenomena of aeroacoustic and aerodynamic origins generated while a train passes by a tunnel.

2. PREDICTION METHODS OF MICRO-PRESSURE WAVE

The new prediction method for the tunnel sonic boom is a combined CFD–Kirchhoff formulation, consisting of nearfield flow solver based on CFD and Kirchhoff integral formulation. The Euler equation is used to analyze the flow-field originating from the aerodynamic interaction of train and tunnel. The flow-field information obtained by CFD is then used in the classical linear Kirchhoff formula to predict the farfield acoustics.

2.1. CFD TECHNIQUE

2.1.1. *Numerical algorithm*

An unsteady, compressible and three-dimensional Euler equation is solved to analyze the flow-field around the high-speed train. The system of equations consists of a local time derivative term and three convective flux vectors. In physical co-ordinates, the governing equation is

$$\frac{\partial Q}{\partial t} + \frac{\partial E}{\partial x} + \frac{\partial F}{\partial y} + \frac{\partial G}{\partial z} = 0, \qquad (1)$$

where

$$Q=\begin{pmatrix}\rho\\ \rho u\\ \rho v\\ \rho w\\ \rho e\end{pmatrix}\quad E=\begin{pmatrix}\rho u\\ \rho u^2+p\\ \rho uv\\ \rho uw\\ (\rho e+p)u\end{pmatrix}\quad F=\begin{pmatrix}\rho v\\ \rho uv\\ \rho v^2+p\\ \rho vw\\ (\rho e+p)v\end{pmatrix}\quad G=\begin{pmatrix}\rho w\\ \rho uw\\ \rho vw\\ \rho w^2+p\\ (\rho e+p)w\end{pmatrix}.$$

The equation of state is as follows:

$$e=\frac{1}{\rho(\gamma-1)}p+\frac{1}{2}(u^2+v^2+w^2), \tag{2}$$

where γ is the ratio of specific heats.

Roe's finite volume flux difference splitting technique based upon the solution of the Riemann problem [10] is used for spatial discretization and monotone upstream-centered scheme conservation laws (MUSCL) with van Albada flux limiter is used to achieve the third order spatial accuracy. Calculations of unsteady flow-field around a moving body require a time-accurate numerical integration. In the present study, Yoon's LU-SGS [11], an implicit scheme, is chosen for efficient time marching due to the huge demand on computer power for such three-dimensional computation.

2.1.2. *Grid systems*

The grid system for the computation of the three-dimensional train/tunnel interaction is characterized by a moving body confined to linear motions on the rail, relative motions between solid bodies, ground proximity and large computational domain through which a train moves.

To accommodate the relative motion, Fujii [8, 12] used fortified solution algorithm (FSA), while Mestreau [9] used unstructured grid with automatic remeshing. Fujii's approach to the current problem is similar to the Chimera [13] procedure composed of hole construction and linear interpolation at boundaries. To obtain a stable solution, a moderate cell volume ratio between giving cell and target cell has to be maintained at the boundaries. If the region swept by the train is large, a huge number of grid points along the region are required in order to preserve the proper interpolation criterion. Fujii used an intermediate zone to overcome this requirement, the application of which made the linear interpolation routine more complicated. In this study, three types of domain decomposition technique (DDT) were applied: multi-block, patched and overlapping grid to obtain computational efficiency and extensibility. Figure 1 shows the schematic for zone decomposition and the zonal interface for the tunnel entry problem. Zone 1 moves with the high-speed train while zone 2 is a fixed grid. Consequently, a simplified Chimera hole construction and linear interpolation are required at the fore and aft overlapping regions of zones 1 and 2. As there exists no stiff gradient of the flow variables except in the vicinity of the train, and the wave phenomena in the tunnel are nearly one-dimensional, the linear interpolation is sufficiently reliable and does not require a tedious three-dimensional conservative treatment [14]. Zone 3 as an intermediate zone shares a sliding surface with zone 1. Zone 4 is the tunnel entrance zone. At the tunnel exit, we can define zone 5 similar to zone 4. Table 1 lists the number of grid points used to predict the nearfield flow. In the computations, the constant time step of $\Delta t = 0{\cdot}01$/iteration is used. It takes approximately 16 s for 1 iteration at 450 MHz digital Alpha CPU. The time scale is normalized by D/a_∞.

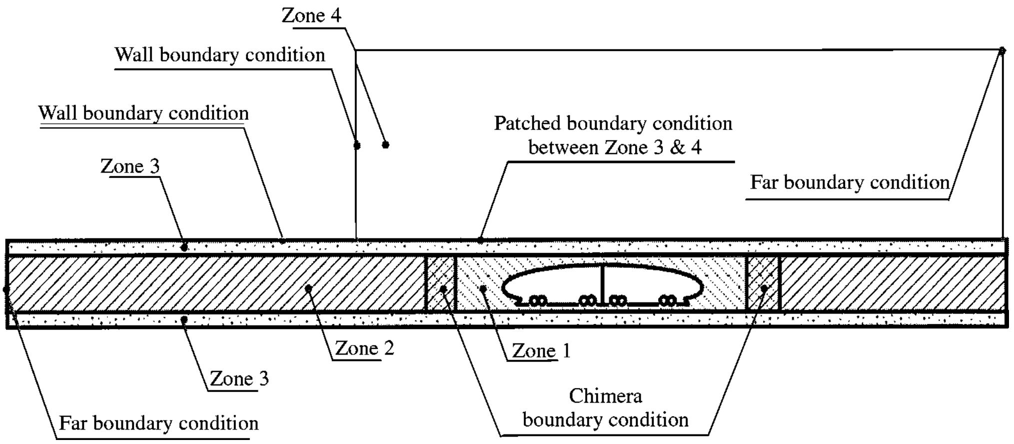

Figure 1. Schematic diagram for zone decomposition and boundary condition.

TABLE 1

Number of grid points used for prediction flow-field

Zone	Grid (x, y, z)	Sum of grid
1	(71, 23, 25)	40 825
2	(441, 23, 25)	247 825
3	(441, 23, 25)	49 565
4	(120, 18, 25)	58 500
5	(40, 18, 25)	18 000
Total sum of grid		410 215

2.2. KIRCHHOFF FORMULATION

The Kirchhoff formulation is applied to predict the micro-pressure wave at the tunnel exit. The nearfield flow data obtained by CFD is used as an input to Kirchhoff formulation. The Kirchhoff integral formula for a stationary control surface is the analytic expression of Huygens' principle [15]. The Kirchhoff equation is

$$p'(\mathbf{x},t) = \frac{1}{4\pi}\iint_S \left[\frac{\cos\theta}{r^2}p' - \frac{1}{r}\frac{\partial p'}{\partial n} + \frac{\cos\theta}{a_\infty r}\frac{\partial p'}{\partial \tau}\right]\mathrm{d}S(\mathbf{y},\tau), \tag{3}$$

where p' is the perturbed pressure; $(\mathbf{x}, t)$ are the observer's location and time; $(\mathbf{y}, \tau)$ are the source location and retarded time variables; θ is the angle between the normal vector $(\mathbf{n})$ on the surface and the radiation vector $(\mathbf{r})$; r is the distance between a source at the retarded time and an observer; and a_∞ is the speed of sound. Note that pressure and its derivatives are calculated at the retarded time, τ. Equation (3) has been widely used for aeroacoustic predictions such as high-speed impulsive noise and transonic blade–vortex interaction noise generated by a rotor [16, 17].

The integration is performed at the control surface called Kirchhoff surface containing the flow-field information. In the present study, the exit plane is considered as the control surface, and an image source of sound is imposed to consider the ground effect. Using a coefficient of sound absorption at the ground, the absorption of the acoustic wave is calculated. The coefficient varies with the frequency of the incident wave and the material property [18]. In this study, the rising time of the compression wave is regarded as the characteristic time. The coefficient is determined with respect to this characteristic time.

3. EXPERIMENT

3.1. DESCRIPTION OF THE EXPERIMENT

The train tunnel facility, depicted in Figure 2, consists of a train model, a pneumatic launcher and a tunnel. After rupturing the driver membrane, the pressurized air accelerates the axisymmetric model train in the launch tube. After leaving the launch tube, the train model can be guided through the tunnel model by using a guidance ring that slides along two piano wires. The models are made of balsa wood except for the noses made of aluminum.

Three different train noses were used in the rig test. All the models were 20 mm in diameter and had a length of 2340 mm. A view of the train and the tunnel model is presented in Figure 3. The tunnel had a rectangular shape of constant height (40 mm) and changeable width. Four different tunnel widths were investigated: 73, 77, 92 and 97 mm, corresponding to a blockage ratio of respectively 10·8, 10·2, 8·5 and 8·1%. Two different tunnel entrances were also used in the test to investigate the effect of the geometry of the tunnel: a 45° slanted and a non-slanted entry. The tunnel lengths were 7640 or 3820 mm. The air-shafts installed to reduce the pressure wave have a lateral distance of 22·9 mm, a length of 66 mm and an internal diameter of 14 mm, positioned at $x = 718, 1436, 2115, 5348, 6974$ and 6807 mm (set $x = 0$ at the entry of the tunnel) for the 7640 mm tunnel.

B&K microphones were used to record the micro-pressure wave. There were placed at 120 and 240 mm from the exit and 20 mm above the ground plate, inclined 45° to the tunnel axis. The diaphragm of each microphone was placed perpendicular to the propagation direction of the micro-pressure waves.

3.2. DATA-ACQUISITION

The measurements were triggered by an accelerometer that was placed on the launch tube. The train speeds before and behind the tunnel were determined from the interrupted signal from light cells placed at a 300-mm interval at the entrance and the exit of the tunnel.

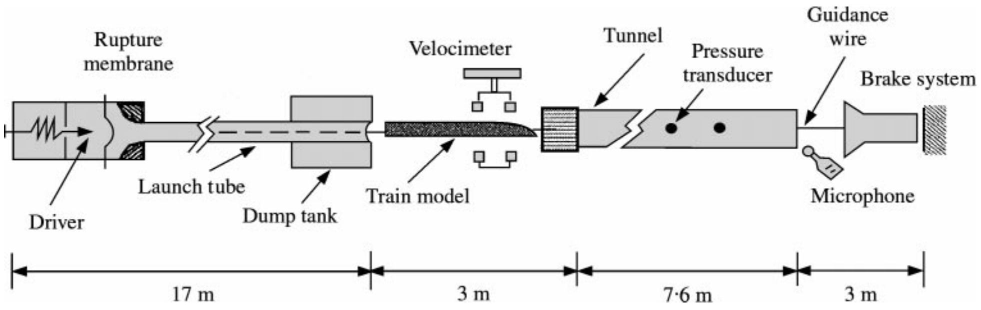

Figure 2. Experimental setup of Train Tunnel Test Facility (T3F) in NLR.

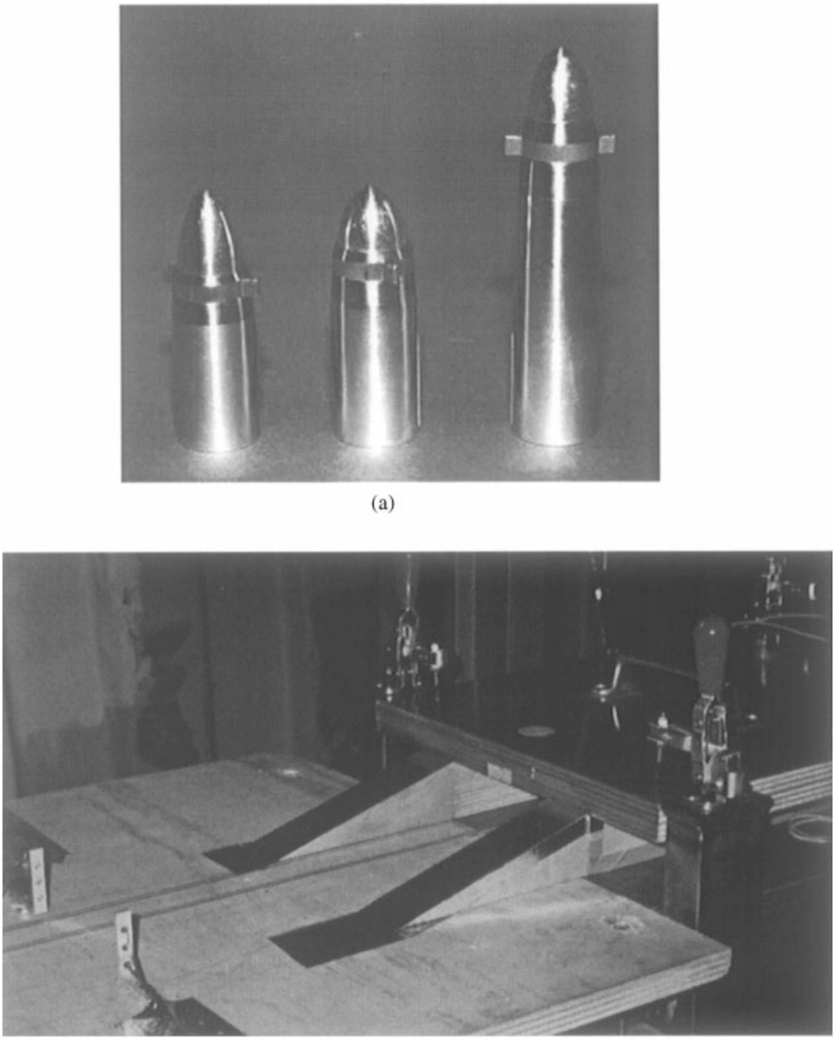

(a)

(b)

Figure 3. A view of the model of the train (a) and the tunnel (b) in rig test.

The pressure fluctuations in the tunnel were recorded simultaneously at 11 positions with pressure transducers (Endevco, type 8510-B2) of 13·8 kPa dynamic range and 70 kHz. For the measurements of the micro-pressure waves, two 1/4-inch microphones (B&K, type 4135) of 3·2 kPa maximum range and 110 kHz resonance frequency were used. The signals were fed to a data acquisition system (Leuven Measurements and Systems), consisting of a DIFA front end (low-pass filtering and analogue to digital conversion) and HP9000/375 computer.

For all the tests, 16 measurement channels were used: they are listed in Table 2 with the locations. The sampling frequency is 81 kHz for each channel. The discrete error of the measured pressure transducer signals was 2·2 Pa, while that for the microphone signals was between 0·2 and 1 Pa.

The entrance speed of the train in the tunnel had to lie within 1·5 m/s from the desired train speed. For a desired train speed of 83·3 m/s, this results in an error in the pressure rise

TABLE 2

Positions of pressure transducers in the tunnel and microphones

Channel number	Type of transducer	Location of transducer
01	Accelerometer	On launch tube
02	Light cell array	300 mm for tunnel
03	Light cell array	At tunnel exit
04	Pressure transducer (No. 1)	332 mm aft entrance
05	Pressure transducer (No. 2)	431 mm aft entrance
06	Pressure transducer (No. 3)	1149 mm aft entrance
07	Pressure transducer (No. 4)	1868 mm aft entrance
08	Pressure transducer (No. 5)	2860 mm aft entrance
09	Pressure transducer (No. 6)	3705 mm aft entrance
10	Pressure transducer (No. 7)	4551 mm aft entrance
11	Pressure transducer (No. 8)	5398 mm aft entrance
12	Pressure transducer (No. 9)	6244 mm aft entrance
13	Pressure transducer (No. 10)	7090 mm aft entrance
14	Pressure transducer (No. 11)	7227 mm aft entrance
15	B&K microphone	120 mm aft exit
16	B&K microphone	240 mm aft exit

TABLE 3

Test types used in rig test

Test type	Model train (mm^2)	Tunnel area (mm^2)	Blockage ratio (%)	Aspect ratio (h_{max}/l_p)
A-1 (K-TGV)	314·2	3680	8·5	10 mm/40 mm
A-2	314·2	2920	10·8	10 mm/40 mm
B-1 (Short nose)	314·2	3880	8·1	10 mm/40 mm
B-2	314·2	3080	10·2	10 mm/40 mm
C-1 (Long nose)	314·2	3880	8·1	10 mm/70 mm
C-2	314·2	3080	10·2	10 mm/70 mm

of the first compression wave of 3·6% (at 105·6 m/s this error is 2·9%). Since the temperature deviation from 292 to 235 K is very small during the measurements, no corrections have been carried out for temperature or other factors.

4. RESULTS AND VALIDATION

4.1. FORMATION OF COMPRESSION WAVE AND GENERATION OF MICRO-PRESSURE WAVE

Cross-sectional areas of each tunnel and train model with blockage ratios and aspect ratios (maximum train height/profiled nose length) are consolidated in Table 3. Figure 4 plots the nose geometry of three models named type A, B and C.

The C-1 model and the non-slanted entry are considered as a representative case. At the speed of 300 km/h the measured pressure fluctuation at $x/L = 24{\cdot}4\%$ is plotted in Figure 5(a) where L is the tunnel length, and the pressure at $x/L = 94{\cdot}6\%$ is represented in

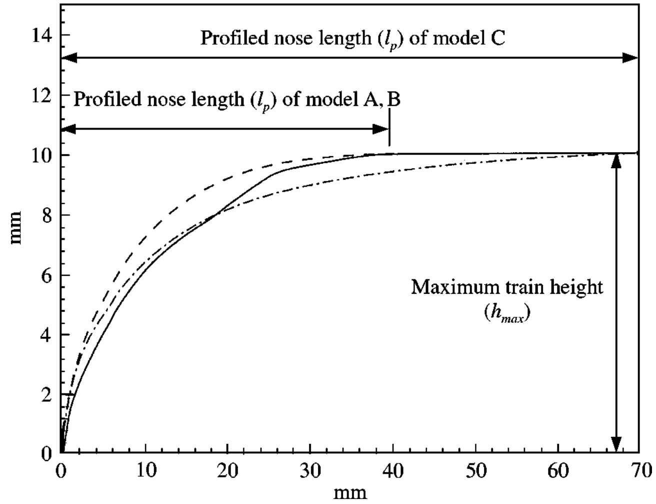

Figure 4. Model of train. Key: ——, train A; ······, train B; –·–·–·, train C.

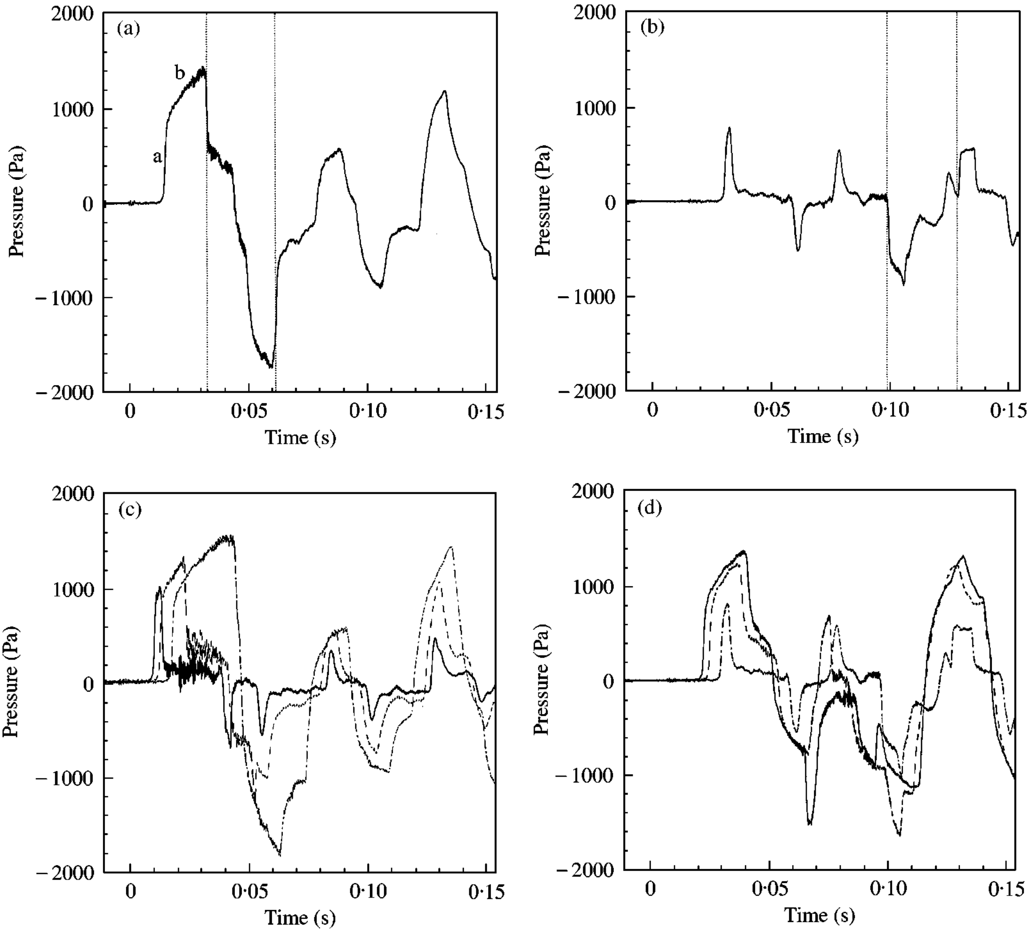

Figure 5. Pressure fluctuations in the tunnel measured at various positions in case of test type C-1 at a speed of 300 km/h: (a) at $x/L = 24{\cdot}4\%$; (b) at $x/L = 94{\cdot}6\%$; (c) at $x/L =$ ——, 4·3%; – – – –, 15%; –·–·–·, 37·4%; (d) at $x/L =$ ——, 59·6%; – – – –, 70·6%; –·–·–·, 92·8%.

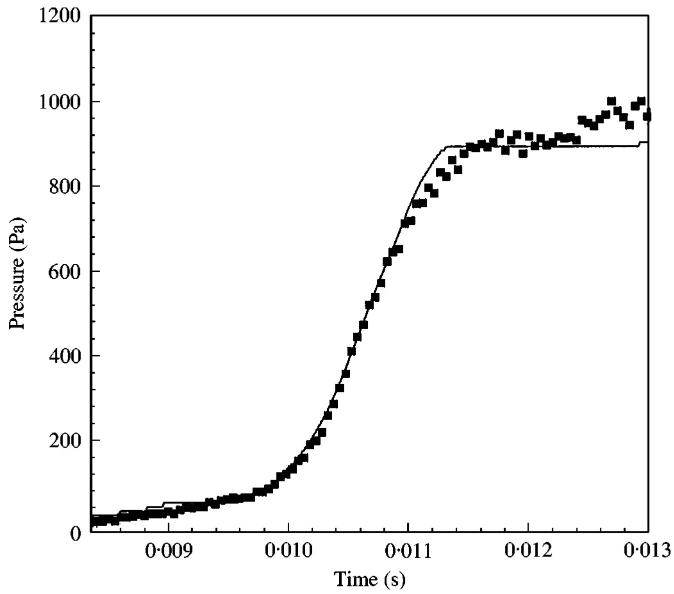

Figure 6. Comparison with measured and predicted entry compression wave in case of test type C-1 having non-slanted entry and for 300 km/h. Key: ——, predicted results; ■, measured data.

Figure 5(b). As soon as the train passes by the tunnel, the compression wave is generated by the abrupt change of cross-sectional area (region a) and the amplitude increases slowly by Reynolds effect (region b) [19]. At the moment the train passes the transducer, the pressure rapidly drops. However, in Figure 5(b), the pressure drops before the passage of the train because the wave front of the compression wave has arrived at the tunnel exit, partially radiating the micro-pressure wave and partially reflecting back as an expansion wave. In Figure 5(a) and (b), the inner part of the dotted line represents the region where the train passes by the pressure transducer. Figure 5(c) and (d) show the measured pressure fluctuations at various positions of the transducer. Figure 5(c) shows that the compression wave becomes stronger as it propagates near the entry, corresponding to the piston principle, while Figure 5(d) illustrates that the compression wave becomes weaker as it propagates toward the exit because of the reflected expansion.

To validate the prediction in the present study, entry compression wave at $x/L = 4{\cdot}3\%$ is compared with the experimental result in Figure 6. At non-dimensional time $t = 0$, the train is located at $x = 9D$, where D is the width of the tunnel. Here, the length scale is normalized by the width of the tunnel. The initial position of the train is determined such that the pressure wave by the impulsive start is sufficiently attenuated by the time the train enters the tunnel. An accurate prediction of the gradient and the amplitude of the compression wave is very important in the prediction of the micro-pressure wave at the tunnel exit because the strength of the micro-pressure wave is proportional to the gradient of the compression wave.

The propagation of the compression wave along the tunnel is numerically simulated in Figure 7(a)–(d) for the case of type C-1 of non-slanted entry with 350 km/h entrance velocity. In Figure 7(a), it is observed that the compression wave is generated before the head of the train enters the tunnel. The compression wave propagates toward the exit of the tunnel faster than the train itself at about the speed of sound: see Figure 7(b) and (c). Finally, in Figure 7(d), the compression wave radiates from the exit as a pulse-like wave called the

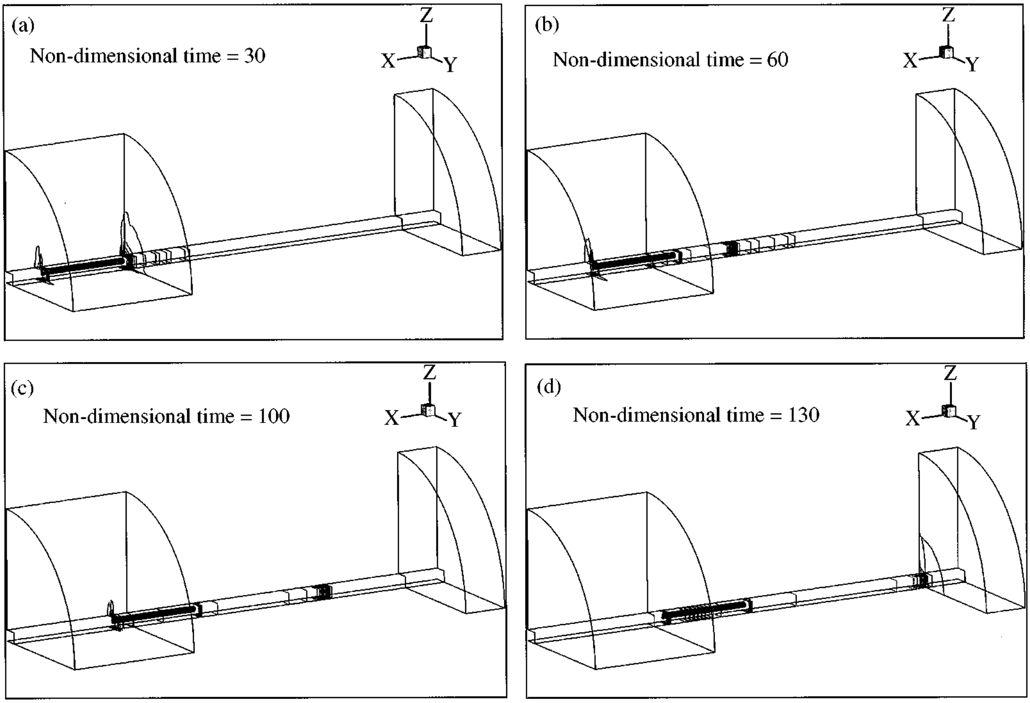

Figure 7. Time series of pressure contour representing the propagation of compression wave in case of test type C-1 having a speed of 350 km/h and non-slanted entry: (a) at time = 30; (b) at time = 60; (c) at time = 100; (d) at time = 130.

micro-pressure wave, and the expansion wave is created at the entrance when the rear end of the train arrives at the tunnel entry.

Figure 8 shows the comparison of the calculated results with experimental data at speeds of 300, 350, and 380 km/h. The measurement positions at the exit are explained in section 3.1. The predicted micro-pressure wave shows a satisfactory agreement in both amplitude and waveform. Therefore, the proposed prediction method, a combined CFD–Kirchhoff method, works very well in analyzing the micro-pressure wave as well as the aerodynamic interaction between the train and the tunnel.

The characteristic of the compression wave is determined not only by the nose shape of the train but also by the geometry of the tunnel entrance. One of the countermeasures to reduce the gradient of the incident compression wave and the micro-pressure wave is the slanted portal. Figure 9 shows the effect of the slanted entry in the case of C-1 with 45° slanted entry and a non-slanted entry at a speed of 350 km/h. In the prediction, the slanted entry was treated as a wall boundary condition. The effect of slanted entry can be thought to prevent the abrupt change of cross-sectional area. As shown in Figure 9, the pressure gradient of the compression wave is not as steep as that of the non-slanted entry.

4.2. PARAMETRIC STUDIES ON THE MICRO-PRESSURE WAVE

The magnitude of the micro-pressure wave depends on parameters such as speed of the train, blockage ratio, train nose and portal shape, length of the tunnel and air-shafts, etc. Figure 10(a) shows the effect of train speed on the micro-pressure wave. The operation

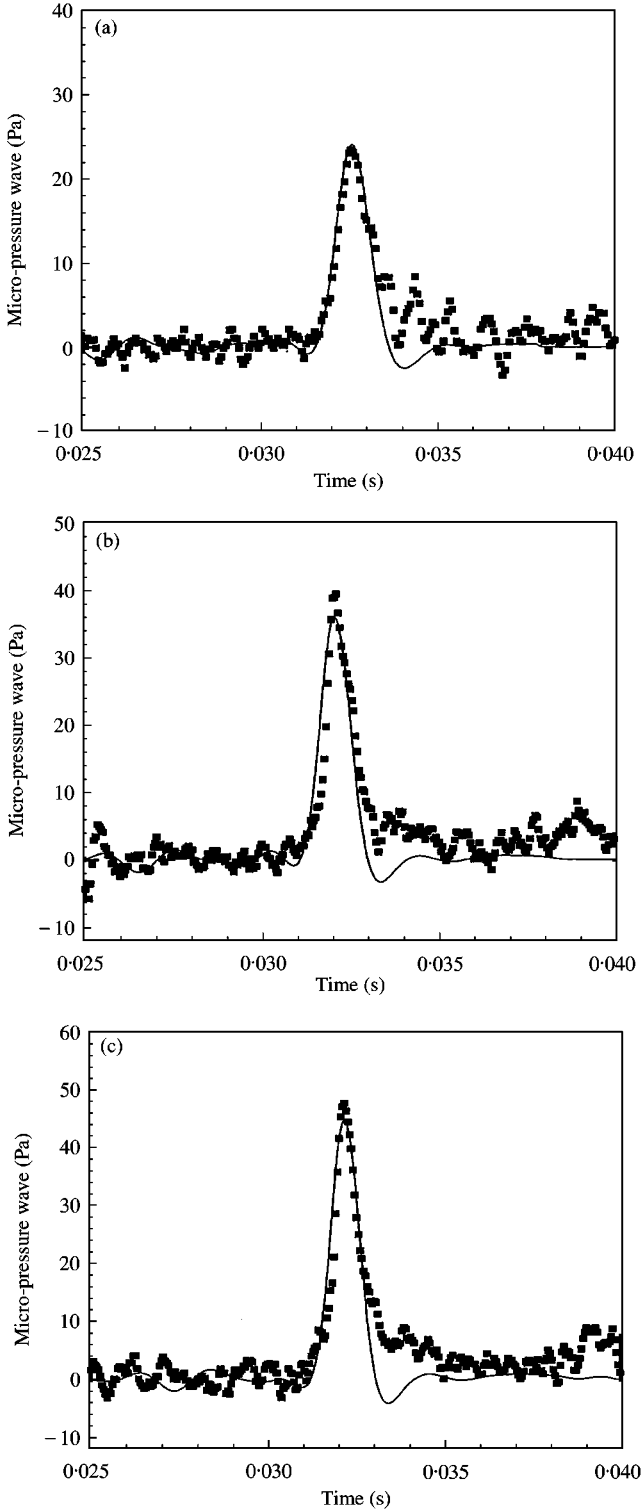

Figure 8. Comparison of predicted and measured micro-pressure wave for (a) 300 km/h, (b) 350 km/h and (c) 380 km/h in case of test type C-1 having non-slanted entry. Key: ——, predicted; ■, measured.

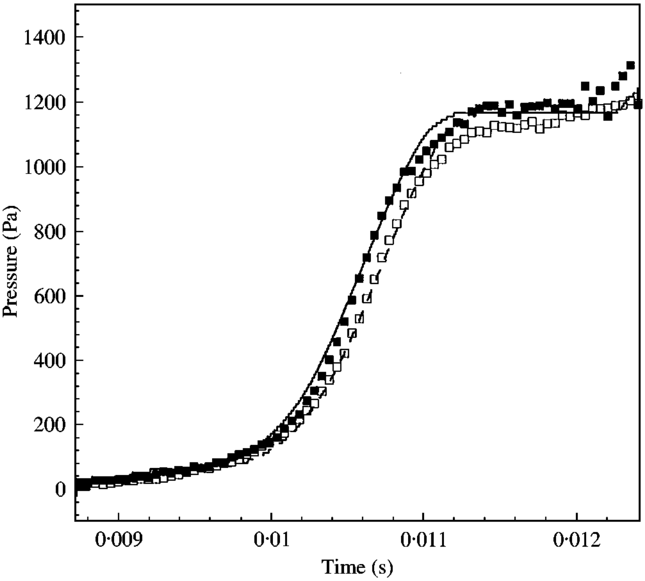

Figure 9. Effect of the slanted entry on incident compression wave at 4·3% from the entry of the tunnel in case of test type C-1 at a speed of 350 km/h. Key: ——, predicted (non-slanted entry); ----, predicted (45° slanted); ■, measured (non-slanted); □, measured (45° slanted).

model is test type C-1 with a non-slanted and a 45° slanted entry. As shown in Figure 10(a), the strength of the micro-pressure wave becomes stronger as the train runs faster. In the case of 45° slanted entry, the intensity of the micro-pressure wave is weaker than in non-slanted entry at comparatively low velocities, but the situation is reversed at the high velocity of 380 km/h. Figure 10(b) shows the effect of blockage ratio on the micro-pressure wave in case of test type C-1 with a 45° slanted entry. As the blockage ratio increases, the micro-pressure also increases.

Figure 11(a) compares the effect of the train nose shape on the micro-pressure wave in case of test types A-1, B-1 and C-1 with 45° slanted entry. The relatively long nose shape (type C) generates a smaller micro-pressure wave than the short nose shape (type B) for the same blockage ratio. Maeda *et al.* suggested that an effective nose shape should have a small deviation of the cross-sectional area [6]. From the result in Figure 11(a), even though type A produces maximum micro-pressure wave at 300 km/h, the increase of farfield noise versus the speed of the train is milder than that of the other types. The tunnel length also has an influence on the micro-pressure wave. In Figure 11(b) which shows type C-1 and a 45° slanted entry, the micro-pressure wave in a short tunnel is stronger in the whole range of speed. This is because the track structure in the rig test has a property of ballasted track. In general, it is known that the ballasted track can be regarded as a porous sound-absorbing material that is effective in the low-frequency range. The penetration of the air in the tunnel into the ballasted track gives rise to the dissipation and the dispersion of compression waves [1].

Air-shafts of the tunnel are known to be an effective countermeasure for the reduction of pressure fluctuation and the corresponding micro-pressure wave. For instance, Burri and Zumsteg [20] tested the influence of air-shafts on the maximum pressure fluctuation inside the tunnel, reporting that the air-shafts could reduce up to 40% of resultant noise. In this study, the effects of air-shafts were examined with two, four and six air-shafts, the locations

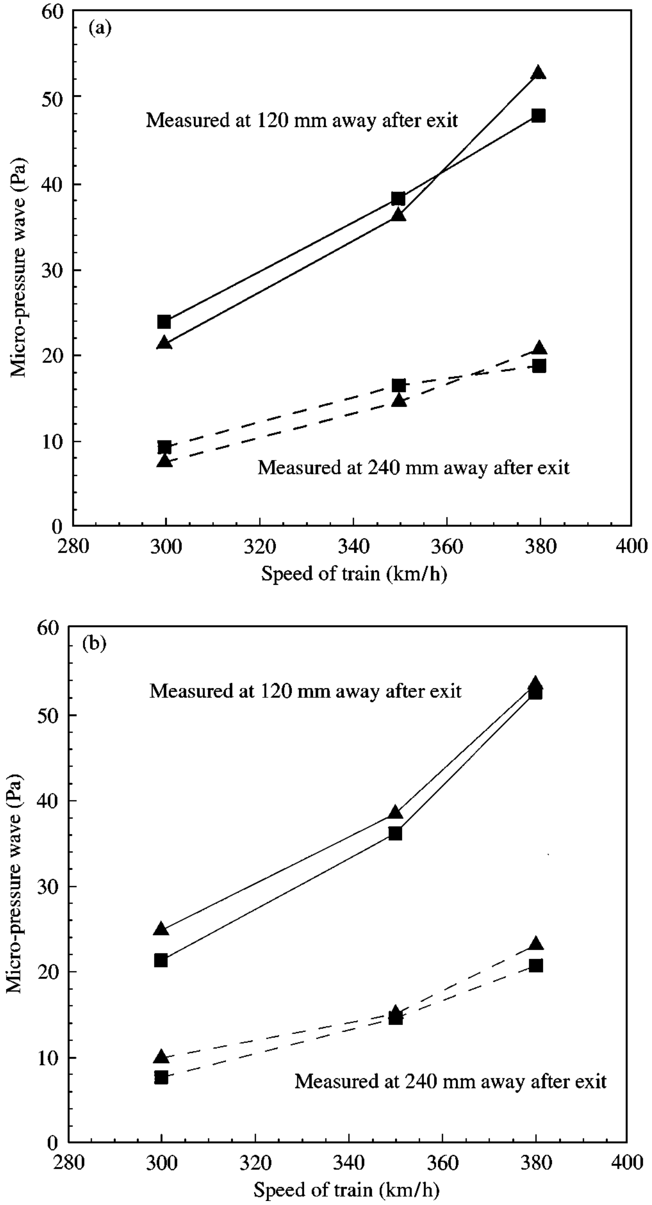

Figure 10. Effect of train speed and blockage ratio on micro-pressure wave. (a) Effect of the speed of train on micro-pressure wave in case of test type C-1 having non-slanted and 45° slanted entry. Key: ■, non-slanted entry; ▲, 45° slanted entry. (b) Effect of blockage ratio on micro-pressure wave in case of test type C-1 and C-2 having 45° slanted entry. Key: ■, blockage ratio of 8·1%; ▲, blockage ratio of 10·2%.

and the sizes of which were referred to in section 3.1., and compared with the case of no air-shaft. Figure 12(a) and (b) show the effect of the air-shaft on the micro-pressure wave in case of the types C-1 and C-2 at train speeds of 300 and 350 km/h respectively. The measurements imply that air-shafts can be an effective countermeasure for reducing the micro-pressure wave instead of the expensive expansion of the tunnel cross-section.

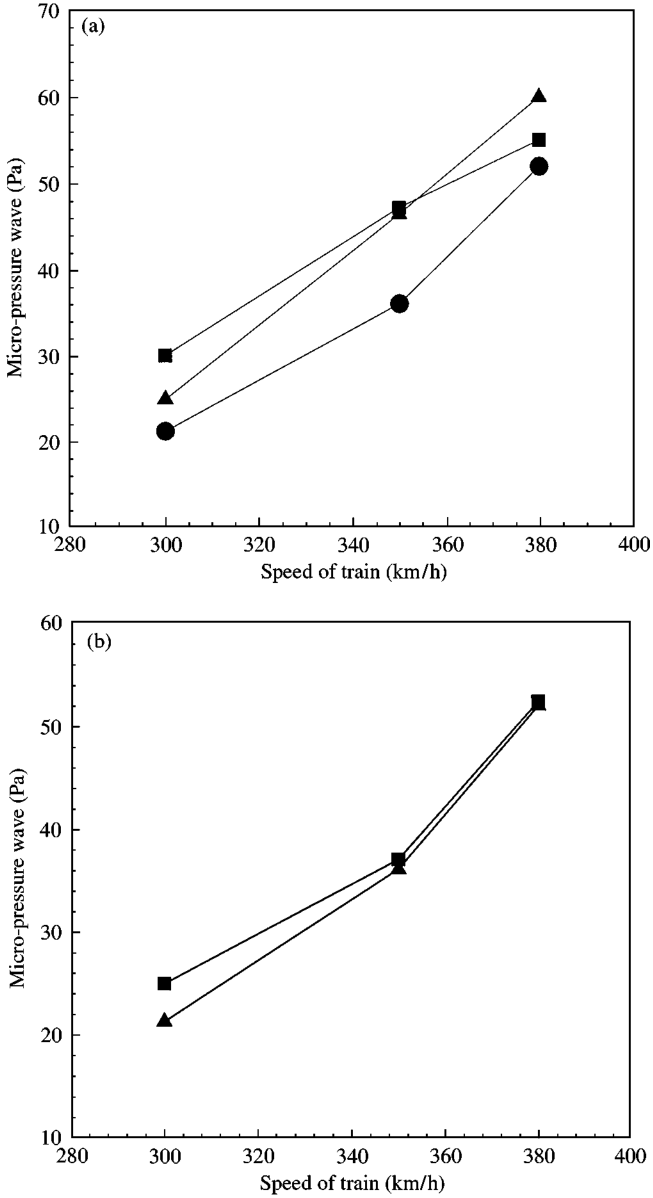

Figure 11. Effect of train nose shape and tunnel length on micro-pressure wave. (a) Effect of shape of the train on micro-pressure wave in case of test type C-1 having 45° slanted entry. Key: —■—, test type A-1; —▲—, test type B-1; —●—, test type C-1. (b) Effect of length of the tunnel on micro-pressure wave in case of test type C-1 having 45° slanted entry. Key: —■—, a length of 3820 mm; —▲—, 7640 mm.

5. CONCLUSION

A novel method is attempted in predicting the micro-pressure wave generated at the tunnel exit when the high-speed train passes by the tunnel. The results are compared with the experimental data in T3F facility in NLR. The three-dimensional inviscid numerical

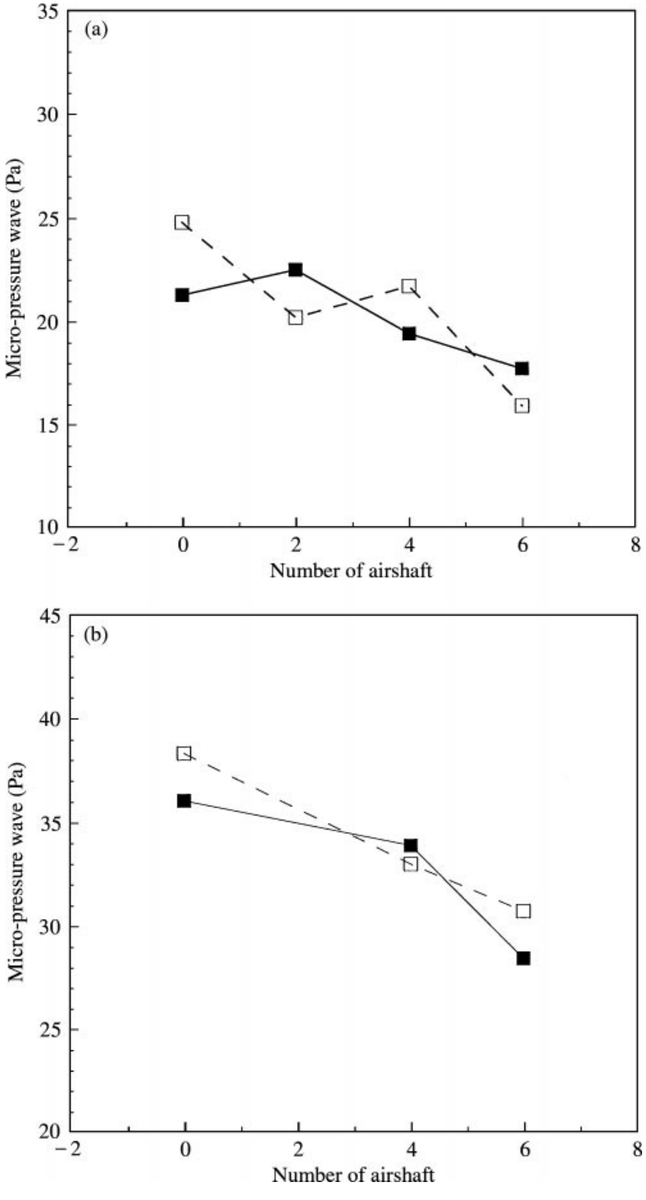

Figure 12. Effect of slanted entry and air-shaft on micro-pressure wave. (a) Effect of air-shafts on the micro-pressure wave in case of test type C at a speed of 300 km/h. Key: —■—, blockage ratio of 8·1%; - - -□- - -, blockage ration of 10·2%. (b) Effect of air-shafts on the micro-pressure wave in case of test type C at a speed of 350 km/h. Key: —■—, blockage ratio of 8·1%; - - -□- - -, blockage ration of 10·2%.

method based on Domain decomposition technique (DDT) is applied to analyze the nearfield fluid dynamics, and the linear Kirchhoff formulation is used to predict the micro-pressure wave. The agreement was found to be good in both the compression wave and the micro-pressure wave. In addition, through the experimental parametric investigation, several strategies of countermeasures have been validated for the efficient reduction of micro-pressure waves.

ACKNOWLEDGMENTS

The authors would like to express their sincere appreciation to E. A. Demmenie and W. B. de Wolf at National Aerospace Laboratory NLR in Netherlands for their technical support of the experiments in the paper. The authors also appreciate the financial support from the Korean government. This is a partial result of 'Aerodynamic Design and Analysis of High-Speed Railway Systems'.

REFERENCES

1. S. Ozawa 1979 *Report of Railway Technical Research Institute*, No. 1121 (in Japanese). Studies of micro-pressure wave radiated from a tunnel exit.
2. S. Ozawa, T. Uchida and T. Maeda 1978 *Quarter Report of Railway Technical Research Institute* **19**, 77–83. Reduction of micro-pressure wave radiated from tunnel exit by hood at tunnel entrance.
3. S. Ozawa, T. Maeda, T. Matsumura, K. Uchida, H. Kajiyama and K. Kanemoto 1991 *in Aerodynamics and Ventilation of Vehicle Tunnels*, 253–266. Oxford: Elsevier Science. Countermeasures to reduce micro-pressure waves radiating from exits of Shinkansen tunnels.
4. A. Yamamoto 1977 *Preprint of Physical Society of Japan* No. 4, 4p-H-4 (in Japanese). Micro-pressure wave radiated from tunnel exit.
5. M. Iida, T. Matumura, K. Nakatani, T. Fukuda and T. Maeda 1997 *Quarter Report of Railway Technical Research Institute* **38**, 206–211 (in Japanese). Effective nose shape for reducing tunnel sonic boom.
6. T. Maeda, T. Matsumura, M. Iida, K. Nakatani and K. Uchida 1993 in *Proceedings of the International Conference on Speedup Technology for Railway and Maglev Vehicles, Yokohama, Japan*, 315–319. Effect of shape of train nose on compression wave generated by train entering tunnel.
7. M. S. Howe, 1998 *Journal of Sound and Vibration* **212**, 23–26. Mach number dependence of the compression wave generated by a high-speed train entering a tunnel.
8. T. Ogawa and K. Fujii 1994 *Computational Fluid Dynamics Journal* **3,** 63–82. Numerical simulation of compressible flows induced by a train moving into a tunnel.
9. E. Mestreau, R. Lohner and S. Aita *American Institute of Aeronautics and Astronautics* 93-0890. TGV tunnel entry simulations using a finite element code with automatic remeshing.
10. P. L. Roe 1981 *Journal of Computational Physics* **43**, 357–372. Approximate Riemann solvers, parameter vectors and difference schemes.
11. A. Jameson and S. Yoon 1987 *American Institute of Aeronautics and Astronautics Journal* **25**, 929–935. Lower–upper implicit schemes with multiple grids for the Euler equations.
12. K. Fujii 1992 *ISAS Report* No. 648, December. Unified zonal method based on the fortified solution algorithm.
13. J. L. Steger, F. C. Dougherty and J. A. Benek 1983 in *Advances in Grid Generation*, FED (K. N. Ghia, editor) Vol. **5**, 59–69. New York: American Society of Mechanical Engineers. A Chimera grid scheme.
14. M. M. Rai and K. Hessenius *American Institute of Aeronautics and Astronautics*-86-1081. Three dimensional conservative Euler computations using patched grid system and explicit methods.
15. B. B. Bakerand and E. T. Copson 1953 *The Mathematical Theory of Huygens' Principle*. Oxford: Clarendon.
16. S. Lee, J. Kim, Y. H. Yu and M. P. Isom 1997 *Journal of Sound and Vibration* **207**, 453–464. Prediction of rotor high-speed impulsive noise with a combined CFD–Kirchhoff method.
17. Y. Xue and A. S. Lyrintzis 1993 *49th Annual Forum of the America Helicopter Society, St. Louis, MO*, The use of rotating Kirchhoff formulation for 3-d transonic BVI far-field noise.
18. C. M. Harris 1991 *Handbook of Acoustical Measurements and Noise Control*. New York: McGraw-Hill.
19. W. Wolf and E. Demmenie 1997 *Nineth International Conference on Aerodynamics and Ventilation of Vehicle Tunnels*; *Aosta Valley, Italy*. A new test facility for the study of interacting pressure waves and their reduction in tunnels for high-speed trains.
20. J. Burri and F. Zumsteg 1997 *Nineth International Conference on Aerodynamics and Ventilation of Vehicle Tunnels*; *Aosta Valley, Italy*. Airshafts for the alleviation of pressure waves in tunnels of the New Swiss Rail 2000.

APPENDIX A: NOMENCLATURE

a_∞	speed of sound
D	width of tunnel
e	total energy per unit volume
p^i	acoustic pressure
L	length of tunnel
h_{max}	maximum train height
l_p	length of profiled nose
r	distance between a source position at the sound generation time and an observer at the sound receiving time
x, y, z	cartesian co-ordinates
u, v, w	velocity components in x, y, z direction
t	observer time
γ	ratio of specific heat
ρ	density
$\mathbf{n}$	normal vector on the surface
θ	angle between the normal vector on the surface and the radiation vector
τ	retarded time
Δt	computational time step